

Thermal and Electronic Properties of Ba_2MnSe_3

Oluwagbemiga P. Ojo, Wilarachchige D. C. B. Gunatilleke, Adam J. Biacchi, Hsin Wang, and George S. Nolas*



Cite This: *Inorg. Chem.* 2023, 62, 3555–3561



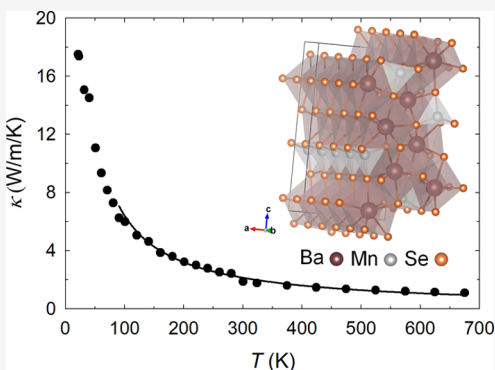
Read Online

ACCESS |

Metrics & More

Article Recommendations

ABSTRACT: The structural, thermal, and electronic properties of Ba_2MnSe_3 were investigated. Analysis of the low-temperature heat capacity revealed a low Debye temperature and a low average speed of sound that, together with the bonding in this material, result in a low thermal conductivity over a relatively large temperature range. Density functional theory and calculated electron localization were employed to investigate the electronic structure and bonding. Absorption and photoluminescence spectroscopy measurements corroborated our calculations and revealed a direct band gap of 1.75 eV. This study expands on our understanding of the physical properties of this material and reveals previously unascertained properties, the knowledge of which is imperative for any potential application of interest.



INTRODUCTION

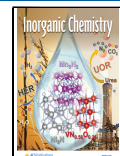
Multinary metal chalcogenides form in a variety of structure types and exhibit varying properties depending on the composition, crystal structure, chemical bonding, and/or processing conditions. These materials continue to be investigated for different applications of interest, including optoelectronics and photovoltaics,^{1–6} superconductivity,^{7–9} topological insulators,^{10,11} thermoelectrics,^{12–15} optical phase-change memory devices,^{16–18} thermal storage devices,^{19,20} and thermal barrier coatings.^{21,22} Among the varying ternary compounds thus far reported are chalcogenides of the form Ba_2XQ_3 (where X = Mn, Cd, Co, Fe, or Zn and Q = S or Se). These ternary chalcogenides possess an orthorhombic crystal structure consisting of linear chains of X atoms formed by corner-sharing XQ_4 tetrahedra, with alkaline earth atoms (coordinated to seven chalcogens) between the chains.^{23–27} They have been employed for fundamental studies of low-dimensional magnetic interactions in solids, where the bridging chalcogens mediate magnetic coupling between the transition metals.^{27–34} In addition, Ba_2XQ_3 chalcogenide compounds have received attention as potential high-temperature superconductors^{30,32} and tunable light-emitting diode materials.^{35–38} Moreover, because antiferromagnetic materials are of interest for high-density data storage and ultrafast switching,^{39–44} certain compositions are currently of interest for possible spintronic applications.

It is noteworthy that the reports mentioned above lack detailed studies of the thermal properties. The thermal properties of materials are among the most fundamental, the knowledge of which is essential for any applications of interest, including those outlined above. Moreover, an intrinsically low

thermal conductivity, κ , is important for thermoelectric, thermal barrier coating and phase-change memory materials with specific structural features such as weak bonding,^{13,45} coordination preferences,^{13,46} lone pair electrons,^{47–50} the large number of atoms per unit cell,^{51,52} the superionic transition,^{53–55} partial occupancy,^{56–59} and strong anharmonicity,^{60–63} leading to low κ values. Motivated by these considerations and our ongoing interest in multinary metal chalcogenides, we investigated the thermal and electronic properties of Ba_2MnSe_3 . To the best of our knowledge, only the magnetic properties of Ba_2MnSe_3 have previously been reported.²⁷ In addition, Ba_2MnSe_3 is of interest due to its low-dimensional, high-spin antiferromagnetic behavior.^{27,34} Moreover, magnetic cations, such as Mn^{2+} , with large and antiparallel spins resulting in bonding heterogeneity may induce low κ values. In addition to temperature-dependent κ and heat capacity measurements, density functional theory (DFT) calculations of the electronic band structure and the calculated electron localization provided further insight into the properties of this material, with ultraviolet–visible (UV–vis) and photoluminescence spectroscopy corroborating the calculated energy band gap of this material.

Received: November 16, 2022

Published: February 15, 2023



EXPERIMENTS AND COMPUTATIONAL METHODS

Phase-pure Ba_2MnSe_3 was synthesized by reaction of BaSe , Mn , and Se . All preparations were carried out inside a N_2 -filled glovebox. Binary BaSe was prepared by the direct reaction of Ba pieces (99.2%, Alfa Aesar) and Se powder (99.999%, Alfa Aesar) combined in a stoichiometric ratio at 1213 K for 3 days.⁶⁴ BaSe , Mn powder (99.99%, Alfa Aesar), and Se powder (99.999%, Alfa Aesar) were placed in a silica ampule in a 2:1:1 stoichiometric ratio that was then placed in a quartz tube. The quartz tube was evacuated and sealed before being placed in a resistive furnace for reaction. The temperature was increased at a rate of 20 K/h to 1123 K, kept at this temperature for 4 days, and then slowly decreased to 723 K at a rate of 2 K/h before decreasing to room temperature at a rate of 10 K/h. The specimen was ground into a fine powder and sieved (325 mesh) before being loaded into a custom-designed WC die-and-punch assembly for densification by spark plasma sintering (SPS, Thermal Technology model 10-3). To prevent reaction with the material, the WC assembly was lined with graphite foil. Densification was accomplished at 673 K and 400 MPa for 30 min under vacuum, resulting in a dense polycrystalline material (96% of the theoretical density). The temperature ramp rate was 25 K min⁻¹, and the pulse:current ratio was 40:1. A TA Instruments Q600 instrument was used for differential thermal analysis (DTA) measurements prior to the SPS densification.

Crystal structure characterization was accomplished by X-ray diffraction (XRD) and Rietveld structure refinement. A Bruker-AXS D8 Focus diffractometer in Bragg–Brentano geometry with $\text{Cu K}\alpha$ radiation and a graphite monochromator was used to collect the powder XRD data, and the GSAS II software package⁶⁵ was used to perform Rietveld refinement. Scanning electron microscopy (SEM) and energy dispersive X-ray spectroscopy (EDS) were used to investigate the grain morphology and the homogeneity of the densified specimen. Optical micrographs were recorded on a SEM instrument (JEOL JSM-6390LV) equipped with an Oxford INCA X-Sight 7582M instrument for EDS. UV–vis–near-infrared (NIR) absorbance spectroscopy was performed in transmission mode using a Cary 5000 spectrophotometer equipped with PMT/PbS detectors. The band gap was determined by a Tauc plot. Photoluminescence spectra were recorded using a Renishaw inVia microscope with 633 nm HeNe laser excitation and emission detection on a 1 in. CCD spread off a 1200 lines/mm grating.

The thermal diffusivity, α_{th} , was measured, from 300 to 675 K, on a 1.0 mm thick 1.3 mm diameter disk utilizing the laser flash technique (NETZSCH LFA457 system) under an Ar flow, with an experimental uncertainty of $\pm 5\%$. The κ values were then calculated according to the relation $\kappa = D\alpha_{\text{th}}C_v$, where D is the density of the specimen and C_v is the isochoric heat capacity estimated from the Dulong–Petit limit $C_v = 3nR$, with n being the number of atoms per formula unit and R the gas constant. A 2 mm \times 2 mm \times 5 mm bar was cut from the densified pellet for low-temperature steady-state κ measurements from 20 to 300 K on a custom-built radiation-shielded vacuum probe with a maximum experimental uncertainty of 8%.^{66,67} Temperature-dependent isobaric heat capacity, C_p , data were measured on a Quantum Design Physical Property Measurement System using thermal N-grease and appropriate addenda. The maximum uncertainty in the entire temperature range was estimated to be 5%.

Ab initio DFT calculations based on self-consistent Kohn–Sham equations were performed as implemented in the Quantum Espresso package⁶⁸ using the structural information from our refinement result. The Perdew–Burke–Ernzerhof^{69,70} plus Hubbard⁷¹ (PBE + U) exchange-correlation functional with projector-augmented waves (PAW) pseudopotentials⁷² was applied. The U parameter was set to 4.7 eV for Mn on the basis of prior studies that provided good agreement between calculated and experimental structural data.⁷³ The valence configurations of the pseudopotentials were $5s^25p^66s^2$, $3s^23p^64s^23d^5$, and $4s^24p^4$ for Ba , Mn , and Se , respectively. A k -point mesh of $3 \times 3 \times 3$, a kinetic energy cutoff for wave functions and a charge density of 680 and 4762 eV, respectively, and an energy convergence threshold of 10^{-7} eV were applied for the self-consistent

field (SCF) calculations. The electron localization function (ELF) distribution was analyzed and visualized using Vesta software.⁷⁴

RESULTS AND DISCUSSION

Figure 1 shows the XRD refinement profiles that include the observed, calculated, and difference patterns, as well as Bragg

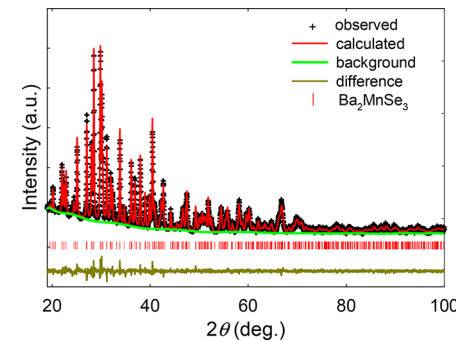


Figure 1. XRD pattern, including the profile fit, profile difference, and Bragg positions.

positions of phase-pure Ba_2MnSe_3 . The refinement results are summarized in Table 1, and the refined atomic positions and

Table 1. Crystallographic Data and Refinement Results

space group	<i>Pnma</i> (No. 62)
<i>a</i> (Å)	9.1546(17)
<i>b</i> (Å)	4.4733(9)
<i>c</i> (Å)	17.764(3)
$\alpha = \beta = \gamma$ (deg)	90
<i>V</i> (Å ³), <i>Z</i>	727.5(4), 4
<i>d</i> (g/cm ³)	5.1724
radiation	graphite-monochromated $\text{Cu K}\alpha$ (1.54056 Å)
2θ range (deg)	19–100
<i>wR</i> _p , <i>R</i> _p	0.05479, 0.04300
goodness of fit	1.436

Table 2. Atomic Coordinates, Occupancies, *f* Values, and Atomic Displacement Parameters (U_{iso})

atom	site	<i>x</i>	<i>y</i>	<i>z</i>	<i>f</i>	U_{iso} (Å ²)
Ba1	4c	0.4198(3)	0.25	0.71366(18)	1	0.021(4)
Ba2	4c	0.2590(4)	0.25	0.45747(16)	1	0.020(4)
Mn	4c	0.3746(7)	0.25	0.1325(4)	1	0.020(5)
Se1	4c	0.9984(5)	0.25	0.60001(25)	1	0.021(4)
Se2	4c	0.3186(5)	0.25	0.27284(27)	1	0.014(4)
Se3	4c	0.1244(5)	0.25	0.07156(28)	1	0.017(4)

isotropic displacement parameters, U_{iso} , are listed in Table 2. The crystal structure, space group *Pnma*, is isostructural with K_2AgI_3 .⁷⁵ There are two crystallographically distinct Ba sites, one Mn site, and three Se sites, with 24 atoms in the unit cell, as shown in Figure 2. Both Ba sites have irregular local environments formed by seven Se atoms in a monocapped trigonal prismatic geometry. The Mn atoms are in a distorted tetrahedron formed by four Se atoms. The BaSe_7 polyhedra and MnSe_4 tetrahedron are connected by common edges to form the complex three-dimensional structure. Selected interatomic bond distances and angles are listed in Table 3.

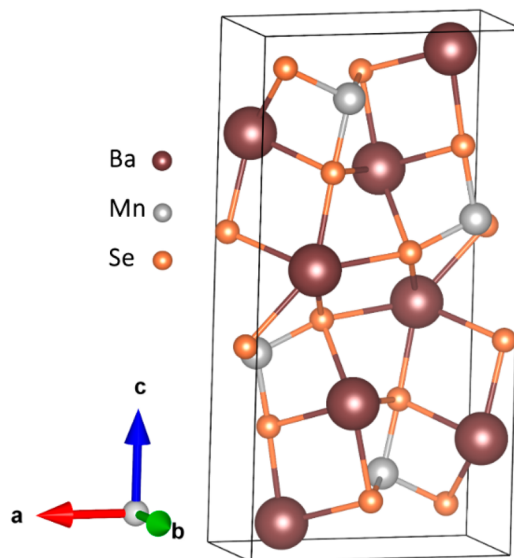


Figure 2. Atom positions within the unit cell.

Table 3. Selected Atomic Bond Lengths (angstroms) and Bond Angles (degrees)

Ba1—Se1	3.387(6)	Se1—Ba1—Se2	80.13(14)
Ba1—Se2	3.297(5)	Se2—Ba1—Se3	72.11(10)
Ba1—Se2	3.286(4)	Se2—Ba1—Se2	157.06(11)
Ba1—Se3	3.397(5)	Se1—Mn—Se1	119.67(30)
Ba2—Se1	3.479(5)	Se1—Mn—Se2	108.03(19)
Ba2—Se2	3.325(6)	Se1—Mn—Se3	108.15(18)
Ba2—Se3	3.202(4)	Se2—Mn—Se3	103.68(26)
Ba2—Se3	3.385(5)	Se1—Ba2—Se1	75.15(12)
Mn—Se1	2.586(4)	Se1—Ba2—Se3	151.57(15)
Mn—Se2	2.545(8)	Se3—Ba2—Se3	76.52(13)
Mn—Se3	2.533(7)	Se3—Ba2—Se3	88.61(14)

Utilizing the atomic bond lengths obtained from our refinement results as well as the bond valence parameters,⁷⁶ empirical bond valence sums of +2.06 and +2.08 were obtained for Ba and Mn, respectively, values that are consistent with an oxidation state of +2 for these ions. Figure 3 shows a SEM micrograph of a cracked surface of the densified specimen revealing the surface morphology with grain sizes in the range of 2–20 μm . The EDS data from a well-polished surface confirmed the stoichiometry from XRD analyses, and elemental mapping (Figure 3) shows the uniform distribution of the constituent elements indicating the good homogeneity of our densified specimen.

Figure 4 shows the DTA data for Ba_2MnSe_3 indicating this material to be stable up to 750 K, with decomposition into BaSe_2 , BaSe , BaSe_3 , and MnSe above this temperature as revealed by XRD of the product after DTA. To determine the optical band gap, as this has not previously been reported for this material, transmission was measured from the NIR to the UV region of the electromagnetic spectrum. From the absorbance, as shown in Figure 5a, the absorption band edge was observed to begin at ~ 2700 nm. A Tauc plot was constructed (inset) by plotting $(\alpha h\nu)^2$ as a function of photon energy $h\nu$. Linear fitting of the steepest gradient provided a value of 1.75 eV for the photonic band gap. The square of the Tauc function provided a good linear fit, indicative of a direct electronic transition. The supposition of a direct band gap was confirmed by photoluminescence spectroscopy, which de-

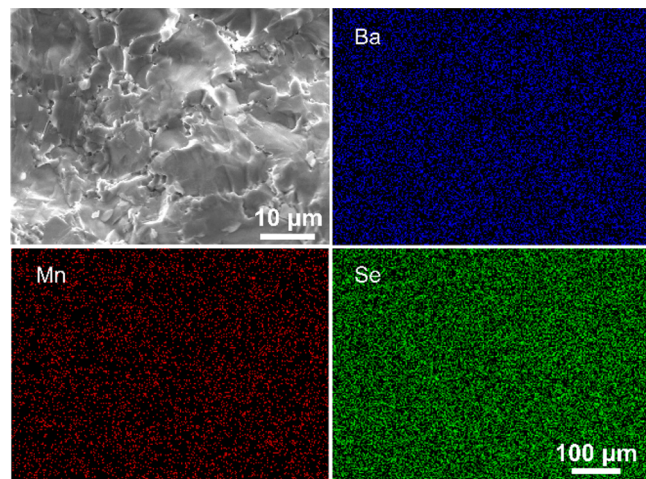


Figure 3. SEM images of a cracked surface and EDS elemental mapping from a well-polished surface illustrating the homogeneity of the specimen, with 35.5(3) atom % Ba, 16.3(4) atom % Mn, and 48.2(4) atom % Se.

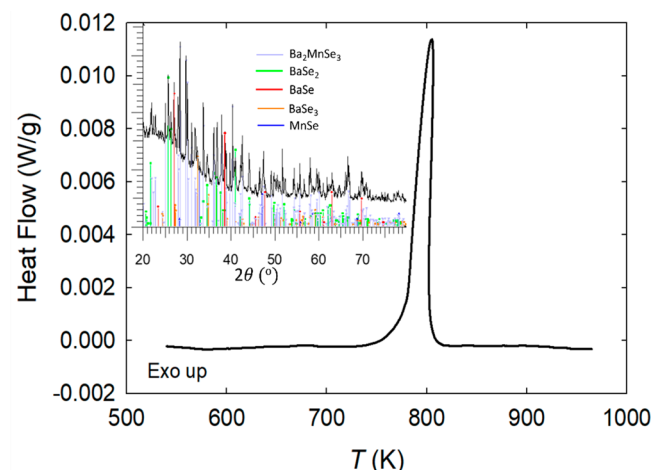


Figure 4. DTA data at a heating rate of 10 K/min indicating that Ba_2MnSe_3 is stable up to 750 K. The inset shows the XRD data after DTA to 773 K indicating decomposition of the main phase into BaSe_2 , BaSe , BaSe_3 , and MnSe .

tected broad emission from Ba_2MnSe_3 upon excitation with a 633 nm HeNe laser, as shown in Figure 5b. Peak emission was detected at 745 nm, corresponding to an energy of 1.66 eV. This is close to, but slightly less than, the optical band gap energy of 1.75 eV, as is normally observed in photoluminescence spectra. Multiple weaker transitions were visible in the photoluminescence spectrum, centered at 827 and 902 nm, suggesting the presence of vibration-assisted relaxation pathways or midgap states.

Thermal conductivity measurements from 20 to 675 K are shown in Figure 6. As shown in the figure, the excellent agreement between the low- and high-temperature data collected on two different specimens that were cut from the same densified pellet is another indication of the homogeneity of the polycrystalline specimen. Due to the relatively large band gap for this material, κ is presumably due to the lattice contribution with negligible, if any, electronic contribution. The κ values are relatively low, ranging from $1.8 \text{ W m}^{-1} \text{ K}^{-1}$ at room temperature to $\sim 1 \text{ W m}^{-1} \text{ K}^{-1}$ above 600 K, with a T^{-1}

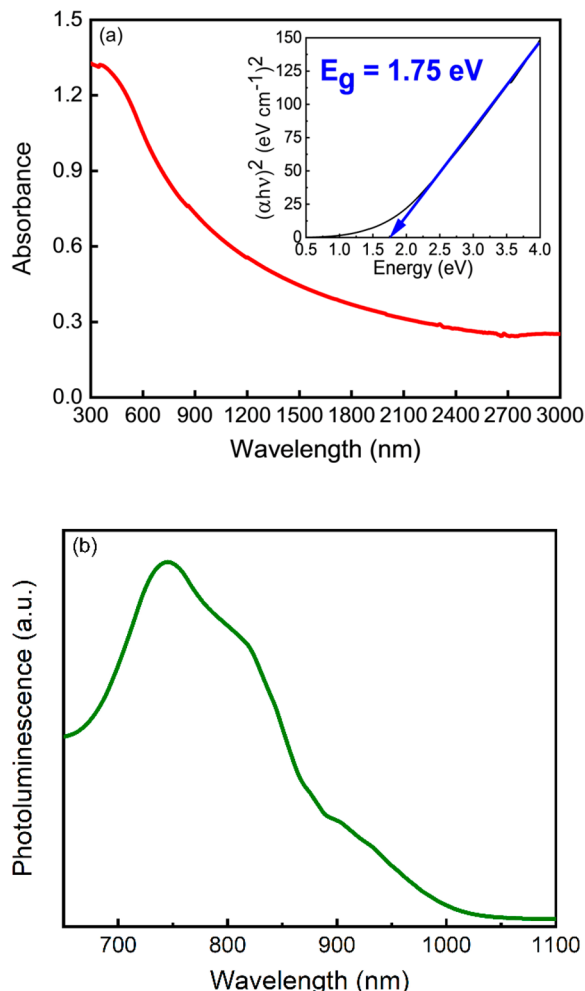


Figure 5. (a) UV–vis–NIR absorbance spectrum, with the corresponding Tauc plot, indicating a direct optical band gap of 1.75 eV and (b) photoluminescence spectra (633 nm excitation) confirming a direct band gap with optical emission peaking at 745 nm.

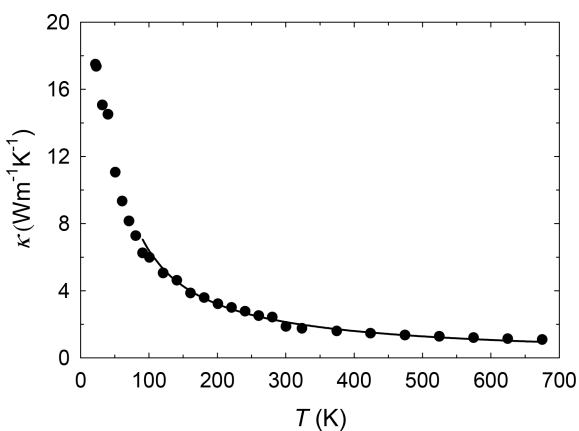


Figure 6. Temperature-dependent κ with a solid line representing a T^{-1} temperature dependence.

temperature dependence indicating Umklapp scattering dominates at higher temperatures.

To gain further insights into the thermal properties, as well as elucidate the reason for the relatively low κ values, heat capacity measurements were also performed. Figure 7 shows the temperature-dependent C_p data for Ba_2MnSe_3 . The C_p data

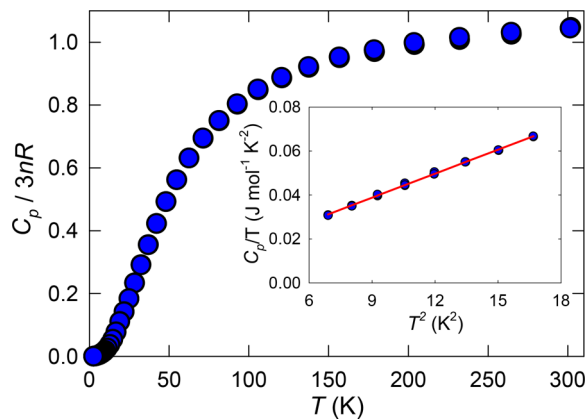


Figure 7. Temperature-dependent $C_p/3nR$ vs T data, where the inset shows C_p/T vs T^2 data at low temperatures with the solid line representing the fit to the relation $C_p/T = \alpha + \beta T^2$.

approach the Dulong–Petit limit at high temperatures, indicating that all of the acoustic and optical phonon modes are fully excited at 300 K. The inset of Figure 7 shows the low temperature data fit to the relation $C_p = \alpha T + \beta T^3$, where the first term represents the electronic contribution and the second term represents the lattice contribution.⁷⁷ The Debye temperature, θ_D , can be determined from the low-temperature C_p data using the relation $\theta_D = (12\pi^4 R n_a / 5\beta)^{1/3}$, where n_a is number of atoms per formula unit and $\beta = 3.6 \text{ mJ mol}^{-1} \text{ K}^{-4}$ from our fit, resulting in a θ_D of 148 K. The average sound speed ($v = 1563 \text{ m/s}$) can be obtained using the relation $\theta_D = v(h/k_B)(3n_a N_a d / 4\pi M_w)^{1/3}$, where h is Planck's constant, k_B is the Boltzmann constant, N_a is Avogadro's constant, d is the density, and M_w is the molecular weight. These relatively low v and θ_D values suggest relatively weak bonds^{13,51,78} in this compound, resulting in a low κ for Ba_2MnSe_3 .

To further consider the bonding in this material and investigate the electronic properties, DFT electronic structure calculations and ELF analyses were performed. As shown in Figure 8, our DFT calculations indicated a direct band gap of 1.8 eV at the Γ point, in very good agreement with our experimentally obtained value. The orbital-projected density of states (DOS) indicated that the valence band maximum (VBM) was mainly composed of Ba 5s6p, Mn 3d, and Se 4p orbitals with contributions from the Se 4p orbital being predominant, while the conduction band minimum (CBM) was mainly from the Mn 3d orbital with slight contributions from Mn 4s, Ba 6s, and Se 4s4p orbitals. The calculated electron localization results are shown in Figure 9. The ELF takes values ranging from 0 (fully delocalized electrons or does not exist) to 1 (perfect localization), with a value of 0.5 corresponding to uniform electron-gas-like pair probability.⁷⁹ From the topological maps, shown in Figure 9, the very low ELF values in the Ba–Se interaction regions indicate that Ba atoms couple to adjacent Se atoms in primarily ionic bonding. In contrast, Mn atoms exhibit spin-dependent electron localization, with primarily ionic and electron-gas-like covalent bonding for Mn2 and Mn1, respectively (see Figure 9). This bonding “heterogeneity” can affect phonon propagation^{80–82} and contribute to the low κ for this material.

CONCLUSION

The thermal and electronic properties of Ba_2MnSe_3 are reported for the first time. Heat capacity data indicated

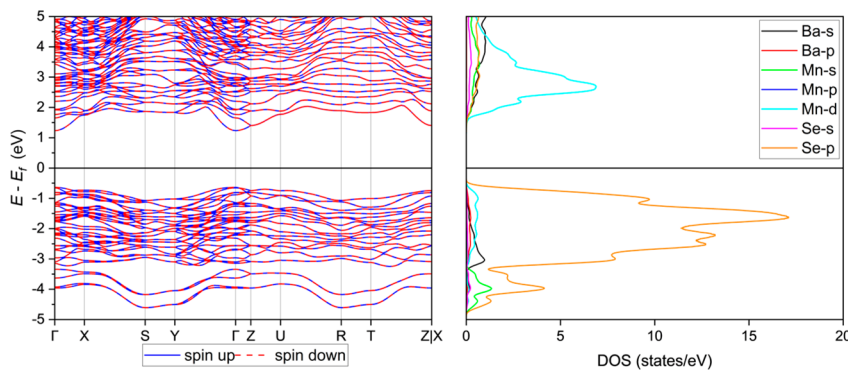


Figure 8. Calculated energy band structure and orbital-projected DOS.

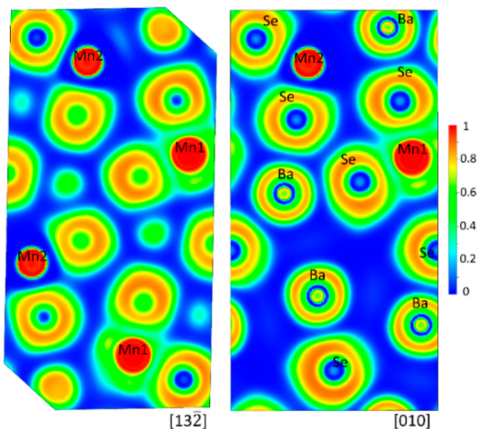


Figure 9. Topological surfaces from calculated ELF. Mn1 and Mn2 correspond to spin-up and spin-down states, respectively.

relatively low θ_D and v values that, together with a relatively complex crystal structure and bonding heterogeneity, lead to a relatively low κ for this ternary chalcogenide. Spectroscopic analyses corroborate the DFT calculations that revealed a relatively large direct band gap with the VBM and CBM mainly composed of Se 4p and Mn 3d orbitals, respectively. The results of this study will be beneficial for improving our understanding of the physical properties of ternary chalcogenides and developing strategies for enhancing specific properties for potential applications of interest in this and similar ternary chalcogenides.

AUTHOR INFORMATION

Corresponding Author

George S. Nolas — Department of Physics, University of South Florida, Tampa, Florida 33620, United States; [orcid.org/0000-0001-8741-1678](#); Email: gnolas@usf.edu

Authors

Oluwagbemiga P. Ojo — Department of Physics, University of South Florida, Tampa, Florida 33620, United States; [orcid.org/0000-0003-1919-6106](#)

Wilarachchige D. C. B. Gunatilleke — Department of Physics, University of South Florida, Tampa, Florida 33620, United States; [orcid.org/0000-0002-8030-8982](#)

Adam J. Biacchi — Nanoscale Device Characterization Division, National Institute of Standards and Technology (NIST), Gaithersburg, Maryland 20899, United States; [orcid.org/0000-0001-5663-2048](#)

Hsin Wang — Materials Science and Technology Division, Oak Ridge National Laboratory, Oak Ridge, Tennessee 37831, United States

Complete contact information is available at:
<https://pubs.acs.org/10.1021/acs.inorgchem.2c04048>

Notes

The authors declare no competing financial interest.

ACKNOWLEDGMENTS

This work was supported, in part, by National Science Foundation Grant DMR-1748188. H.W. acknowledges the support of the U.S. Department of Energy, Office of Energy Efficiency and Renewable Energy, Vehicle Technologies Office, Powertrain Materials Core Program. Oak Ridge National Laboratory is managed by UT-Battelle LLC under Contract DE-AC05000OR22725.

REFERENCES

- (1) Pal, K.; Singh, P.; Bhaduri, A.; Thapa, K. B. Current Challenges and Future Prospects for a Highly Efficient (>20%) Kesterite CZTS Solar Cell: A Review. *Sol. Energy Mater. Sol. Cells* **2019**, *196*, 138–156.
- (2) Ravindiran, M.; Praveenkumar, C. Status Review and the Future Prospects of CZTS Based Solar Cell - A Novel Approach on the Device Structure and Material Modeling for CZTS Based Photovoltaic Device. *Renew. Sustain. Energy Rev.* **2018**, *94*, 317–329.
- (3) Kush, P.; Deka, S. Multifunctional Copper-Based Quaternary Chalcogenide Semiconductors Toward State-of-the-Art Energy Applications. *ChemNanoMat* **2019**, *5* (4), 373–402.
- (4) Sahu, M.; Minnam Reddy, V. R.; Park, C.; Sharma, P. Review Article on the Lattice Defect and Interface Loss Mechanisms in Kesterite Materials and Their Impact on Solar Cell Performance. *Sol. Energy* **2021**, *230*, 13–58.
- (5) Swarnkar, A.; Mir, W. J.; Chakraborty, R.; Jagadeeswararao, M.; Sheikh, T.; Nag, A. Are Chalcogenide Perovskites an Emerging Class of Semiconductors for Optoelectronic Properties and Solar Cell? *Chem. Mater.* **2019**, *31* (3), 565–575.
- (6) Nolas, G. S.; Hassan, M. S.; Dong, Y.; Martin, J. Synthesis, Crystal Structure and Electrical Properties of the Tetrahedral Quaternary Chalcogenides Cu_MInTe₄ (M = Zn, Cd). *J. Solid State Chem.* **2016**, *242*, 50–54.
- (7) Denisov, D. V.; Tsendar, K. D. Application of Chalcogenides for Creation of New Superconductors. *J. Optoelectron. Adv. Mater.* **2003**, *5* (4), 1011–1016.
- (8) Deguchi, K.; Takano, Y.; Mizuguchi, Y. Physics and Chemistry of Layered Chalcogenide Superconductors. *Science and Technology of Advanced Materials*; IOP Publishing, 2012; p 054303.

- (9) Mizuguchi, Y.; Takano, Y. Review of Fe Chalcogenides as the Simplest Fe-Based Superconductor. *J. Phys. Soc. Jpn.* **2010**, *79*, 102001.
- (10) Feng, W.; Xiao, D.; Ding, J.; Yao, Y. Three-Dimensional Topological Insulators in I-III-VI₂ and II-IV-V₂ Chalcopyrite Semiconductors. *Phys. Rev. Lett.* **2011**, *106* (1), 016402.
- (11) Chen, S.; Gong, X. G.; Duan, C. G.; Zhu, Z. Q.; Chu, J. H.; Walsh, A.; Yao, Y. G.; Ma, J.; Wei, S. H. Band Structure Engineering of Multinary Chalcogenide Topological Insulators. *Phys. Rev. B - Condens. Matter Mater. Phys.* **2011**, *83* (24), 245202.
- (12) Dong, Y.; Wang, H.; Nolas, G. S. Synthesis and Thermoelectric Properties of Cu Excess Cu₂ZnSnSe₄. *Phys. status solidi - Rapid Res. Lett.* **2014**, *8* (1), 61–64.
- (13) He, J.; Xia, Y.; Lin, W.; Pal, K.; Zhu, Y.; Kanatzidis, M. G.; Wolverton, C. Accelerated Discovery and Design of Ultralow Lattice Thermal Conductivity Materials Using Chemical Bonding Principles. *Adv. Funct. Mater.* **2022**, *32*, 2108532.
- (14) Wei, K.; Beauchemin, L.; Wang, H.; Porter, W. D.; Martin, J.; Nolas, G. S. Enhanced Thermoelectric Properties of Cu₂ZnSnSe₄ with Ga-Doping. *J. Alloys Compd.* **2015**, *650*, 844–847.
- (15) Ibáñez, M.; Cadavid, D.; Zamani, R.; García-Castelló, N.; Izquierdo-Roca, V.; Li, W.; Fairbrother, A.; Prades, J. D.; Shavel, A.; Arbiol, J.; Pérez-Rodríguez, A.; Morante, J. R.; Cabot, A. Composition Control and Thermoelectric Properties of Quaternary Chalcogenide Nanocrystals: The Case of Stannite Cu₂CdSnSe₄. *Chem. Mater.* **2012**, *24* (3), 562–570.
- (16) Le Gallo, M.; Sebastian, A. An Overview of Phase-Change Memory Device Physics. *J. Phys. D: Appl. Phys.* **2020**, *53* (21), 213002.
- (17) Simpson, R. E.; Fons, P.; Kolobov, A. V.; Fukaya, T.; Krabal, M.; Yagi, T.; Tominaga, J. Interfacial Phase-Change Memory. *Nat. Nanotechnol.* **2011** *68* **2011**, *6* (8), 501–505.
- (18) Bozorg-Grayeli, E.; Reifenberg, J. P.; Asheghi, M.; Wong, H.-S. P.; Goodson, K. E. Thermal Transport in Phase Change Memory Materials. *Annu. Rev. Heat Transfer* **2013**, *16* (1), 397–428.
- (19) Nazir, H.; Batoool, M.; Bolivar Osorio, F. J.; Isaza-Ruiz, M.; Xu, X.; Vignarooban, K.; Phelan, P.; Inamuddin; Kannan, A. M. Recent Developments in Phase Change Materials for Energy Storage Applications: A Review. *Int. J. Heat Mass Transfer* **2019**, *129*, 491–523.
- (20) Han, G. G. D.; Li, H.; Grossman, J. C. Optically-Controlled Long-Term Storage and Release of Thermal Energy in Phase-Change Materials. *Nat. Commun.* **2017** *81* **2017**, *8* (1), 1–10.
- (21) Li, F.; Zhou, L.; Liu, J. X.; Liang, Y.; Zhang, G. J. High-Entropy Pyrochlores with Low Thermal Conductivity for Thermal Barrier Coating Materials. *J. Adv. Ceram.* **2019** *84* **2019**, *8* (4), 576–582.
- (22) Liu, B.; Liu, Y.; Zhu, C.; Xiang, H.; Chen, H.; Sun, L.; Gao, Y.; Zhou, Y. Advances on Strategies for Searching for next Generation Thermal Barrier Coating Materials. *J. Mater. Sci. Technol.* **2019**, *35* (5), 833–851.
- (23) Gopalakrishnan, J.; Nanjundaswamy, K. S. Transition Metal Chalcogenides Exhibiting Quasi-One-Dimensional Behaviour. *Bull. Mater. Sci.* **1983** *S3* **1983**, *5* (3), 287–306.
- (24) Mathew, T.; Rahul K, S.; Sujith, C. P.; Mathew, V. Electronic and Optical Properties of Quasi-1D Barium Zinc Chalcogenides Ba₂ZnX₃ (X = S, Se, Te): A DFT Approach. *Solid State Sci.* **2021**, *113*, 106456.
- (25) Wang, Y. C.; DiSalvo, F. J. Synthesis and Structural Characterization of Ba₂CdTe₃. *J. Solid State Chem.* **1999**, *148* (2), 464–467.
- (26) Iglesias, J. E.; Pachali, K. E.; Steinfink, H. Structural Chemistry of Ba₂CdS₃, Ba₂CdSe₃, BaCdS₂, BaCu₂S₂ and BaCu₂Se₂. *J. Solid State Chem.* **1974**, *9* (1), 6–14.
- (27) Grey, I. E.; Steinfink, H. Crystal Structure of Ba₂MnSe₃, Linear Antiferromagnetism in Ba₂MnX₃ (X = S, Se). *Inorg. Chem.* **1971**, *10* (4), 691–696.
- (28) Nakayama, N.; Kosuge, K.; Kachi, S.; Shinjo, T.; Takada, T. Studies on the Compounds in the Ba-Fe-S System. I. Linear Chain Antiferromagnetism of Ba₂FeS₃ and Related Compounds Ba₂CoS₃ and Ba₂MnS₃. *J. Solid State Chem.* **1980**, *33* (3), 351–356.
- (29) Sujith, C. P.; Joseph, S.; Mathew, T.; Mathew, V. First-Principles Investigation of Structural, Electronic and Optical Properties of Quasi-One-Dimensional Barium Cadmium Chalcogenides Ba₂CdX₃ (X = S, Se, Te) Using HSE06 and GGA-PBE Functionals. *J. Phys. Chem. Solids* **2022**, *161*, 110488.
- (30) Duan, L.; Zhang, J.; Wang, X.; Zhao, Z.; Xiao, C.; Li, X.; Hu, Z.; Zhao, J.; Li, W.; Cao, L.; Dai, G.; Ren, C.; He, X.; Yu, R.; Liu, Q. Q.; Tjeng, L. H.; Lin, H. J.; Chen, C.-T.; Jin, C. High Pressure Phase of Ba₂FeS₃: An Antiferromagnet with One-Dimensional Spin Chains. *J. Alloys Compd.* **2021**, *859*, 157839.
- (31) Headspith, D. A.; Battle, P. D.; Francesconi, M. G. Long-Range Magnetic Ordering in Ba₂CoS₃: A Neutron Diffraction Study. *J. Solid State Chem.* **2007**, *180* (10), 2859–2863.
- (32) Baikie, T.; Maignan, A.; Francesconi, M. G. Linear Antiferromagnetism in Ba₂CoS₃. *Chem. Commun.* **2004**, *4* (7), 836–837.
- (33) Barnes, A. D. J.; Baikie, T.; Hardy, V.; Lepetit, M. B.; Maignan, A.; Young, N. A.; Francesconi, M. G. Magnetic Coupling and Long-Range Order in the Spin-Chain Sulfide Ba₂CoS₃. *J. Mater. Chem.* **2006**, *16* (34), 3489–3502.
- (34) Greaney, M. A.; Ramanujachary, K. V.; Teweldeemedhin, Z.; Greenblatt, M. Studies on the Linear Chain Antiferromagnets: Ba₂MnX₃ (X = S, Se, Te) and Their Solid Solutions. *J. Solid State Chem.* **1993**, *107* (2), 554–562.
- (35) Zhang, X.; Zeng, H.; Su, Q. Mn²⁺-Doped Ba₂ZnS₃ Phosphor as a Potential Luminescent Material for White LEDs. *J. Alloys Compd.* **2007**, *441* (1–2), 259–262.
- (36) Lin, Y.-F.; Chang, Y.-H.; Tsai, B.-S. Synthesis and the Luminescent Properties of Ba₂ZnS₃:Ce,Ag Phosphors. *J. Electrochem. Soc.* **2005**, *152* (9), G698.
- (37) Thiagarajan, P.; Kottaisamy, M.; Rao, M. S. R. Luminescent Properties of near UV Excitable Ba₂ZnS₃:Mn Red Emitting Phosphor Blend for White LED and Display Applications. *J. Phys. D: Appl. Phys.* **2006**, *39* (13), 2701.
- (38) Zhou, M.; Xiao, K.; Jiang, X.; Huang, H.; Lin, Z.; Yao, J.; Wu, Y. Visible-Light-Responsive Chalcogenide Photocatalyst Ba₂ZnSe₃: Crystal and Electronic Structure, Thermal, Optical, and Photocatalytic Activity. *Inorg. Chem.* **2016**, *55* (24), 12783–12790.
- (39) Bodnar, S. Y.; Smejkal, L.; Turek, I.; Jungwirth, T.; Gomonay, O.; Sinova, J.; Sapozhnik, A. A.; Elmers, H. J.; Klaui, M.; Jourdan, M. Writing and Reading Antiferromagnetic Mn₂Au by Néel Spin-Orbit Torques and Large Anisotropic Magnetoresistance. *Nat. Commun.* **2018** *9* (1), 1–7.
- (40) Lebrun, R.; Ross, A.; Bender, S. A.; Qaiumzadeh, A.; Baldrati, L.; Cramer, J.; Bratas, A.; Duine, R. A.; Kläui, M. Tunable Long-Distance Spin Transport in a Crystalline Antiferromagnetic Iron Oxide. *Nat. 2018* *5617722* **2018**, *561* (7722), 222–225.
- (41) Bai, H.; Zhou, X.; Zhou, Y.; Chen, X.; You, Y.; Pan, F.; Song, C. Functional Antiferromagnets for Potential Applications on High-Density Storage and High Frequency. *J. Appl. Phys.* **2020**, *128* (21), 210901.
- (42) Qiu, H.; Zhou, L.; Zhang, C.; Wu, J.; Tian, Y.; Cheng, S.; Mi, S.; Zhao, H.; Zhang, Q.; Wu, D.; Jin, B.; Chen, J.; Wu, P. Ultrafast Spin Current Generated from an Antiferromagnet. *Nat. Phys.* **2020** *173* **2021**, *17* (3), 388–394.
- (43) Jani, H.; Linghu, J.; Hooda, S.; Chopdekar, R. V.; Li, C.; Omar, G. J.; Prakash, S.; Du, Y.; Yang, P.; Banas, A.; Banas, K.; Ghosh, S.; Ojha, S.; Umapathy, G. R.; Kanjilal, D.; Ariando, A.; Pennycook, S. J.; Arenholz, E.; Radelli, P. G.; Coey, J. M. D.; Feng, Y. P.; Venkatesan, T. Reversible Hydrogen Control of Antiferromagnetic Anisotropy in α-Fe₂O₃. *Nat. Commun.* **2021** *121* **2021**, *12* (1), 1–10.
- (44) Ghosh, S.; Manchon, A.; Železný, J. Unconventional Robust Spin-Transfer Torque in Noncollinear Antiferromagnetic Junctions. *Phys. Rev. Lett.* **2022**, *128* (9), 097702.
- (45) Gibson, Q. D.; Zhao, T.; Daniels, L. M.; Walker, H. C.; Daou, R.; Hébert, S.; Zanella, M.; Dyer, M. S.; Claridge, J. B.; Slater, B.; Gaulois, M. W.; Corà, F.; Alaria, J.; Rosseinsky, M. J. Low Thermal

- Conductivity in a Modular Inorganic Material with Bonding Anisotropy and Mismatch. *Science* **2021**, *373* (6558), 1017–1022.
- (46) Mori, T.; Martin, J.; Nolas, G. Thermal Conductivity of YbB₄₄Si₂. *J. Appl. Phys.* **2007**, *102* (7), 073510.
- (47) Nielsen, M. D.; Ozolins, V.; Heremans, J. P. Lone Pair Electrons Minimize Lattice Thermal Conductivity. *Energy Environ. Sci.* **2013**, *6* (2), 570–578.
- (48) Skoug, E. J.; Morelli, D. T. Role of Lone-Pair Electrons in Producing Minimum Thermal Conductivity in Nitrogen-Group Chalcogenide Compounds. *Phys. Rev. Lett.* **2011**, *107* (23), 235901.
- (49) Dong, Y.; Khabibullin, A. R.; Wei, K.; Salvador, J. R.; Nolas, G. S.; Woods, L. M. Bournonite PbCuSbS₃: Stereochemically Active Lone-Pair Electrons That Induce Low Thermal Conductivity. *ChemPhysChem* **2015**, *16* (15), 3264–3270.
- (50) Hobbis, D.; Wei, K.; Wang, H.; Martin, J.; Nolas, G. S. Synthesis, Structure, Te Alloying, and Physical Properties of CuSbS₂. *Inorg. Chem.* **2017**, *56* (22), 14040–14044.
- (51) Ojo, O. P.; Gunatilleke, W. D. C. B.; Wang, H.; Nolas, G. S. Structural and Thermal Properties of Ultralow Thermal Conductivity Ba₃Cu₂Sn₃Se₁₀. *Dalt. Trans.* **2022**, *51* (16), 6220–6225.
- (52) Beekman, M.; Schnelle, W.; Borrmann, H.; Baitinger, M.; Grin, Y.; Nolas, G. S. Intrinsic Electrical and Thermal Properties from Single Crystals of Na₂₄Si₁₃₆. *Phys. Rev. Lett.* **2010**, *104* (1), 018301.
- (53) Liu, H.; Shi, X.; Xu, F.; Zhang, L.; Zhang, W.; Chen, L.; Li, Q.; Uher, C.; Day, T.; Snyder, G. J. Copper Ion Liquid-like Thermoelectrics. *Nat. Mater.* **2012**, *11* (5), 422–425.
- (54) Xiao, C.; Xu, J.; Li, K.; Feng, J.; Yang, J.; Xie, Y. Superionic Phase Transition in Silver Chalcogenide Nanocrystals Realizing Optimized Thermoelectric Performance. *J. Am. Chem. Soc.* **2012**, *134* (9), 4287–4293.
- (55) Wang, C.; Chen, Y. Highly Selective Phonon Diffusive Scattering in Superionic Layered AgCrSe₂. *npj Comput. Mater.* **2020**, *6* (1), 1–6.
- (56) Liu, Z.; Zhang, W.; Gao, W.; Mori, T. A Material Catalogue with Glass-like Thermal Conductivity Mediated by Crystallographic Occupancy for Thermoelectric Application. *Energy Environ. Sci.* **2021**, *14* (6), 3579–3587.
- (57) Stefanoski, S.; Malliakas, C. D.; Kanatzidis, M. G.; Nolas, G. S. Synthesis and Structural Characterization of Na_xSi₁₃₆ ($0 < x \leq 24$) Single Crystals and Low-Temperature Transport of Polycrystalline Specimens. *Inorg. Chem.* **2012**, *51* (16), 8686–8692.
- (58) Lamberton, G. A.; Tedstrom, R. H.; Tritt, T. M.; Nolas, G. S. Thermoelectric Properties of Yb-Filled Ge-Compensated CoSb₃ Skutterudite Materials. *J. Appl. Phys.* **2005**, *97* (11), 113715.
- (59) Beekman, M.; Nolas, G. S. Synthesis and Thermal Conductivity of Type II Silicon Clathrates. *Phys. B Condens. Matter* **2006**, *383* (1), 111–114.
- (60) Chang, C.; Zhao, L. D. Anharmonicity and Low Thermal Conductivity in Thermoelectrics. *Mater. Today Phys.* **2018**, *4*, 50–57.
- (61) Wu, H.; Lu, X.; Wang, G.; Peng, K.; Zhang, B.; Chen, Y.; Gong, X.; Tang, X.; Zhang, X.; Feng, Z.; Han, G.; Zhang, Y.; Zhou, X. Strong Lattice Anharmonicity Securing Intrinsically Low Lattice Thermal Conductivity and High Performance Thermoelectric SnSb₂Te₄ via Se Alloying. *Nano Energy* **2020**, *76*, 105084.
- (62) Ojo, O. P.; Gunatilleke, W. D. C. B.; Poddig, H.; Wang, H.; Martin, J.; Kirsch, D. J.; Nolas, G. S. Synthesis, Structure, Electronic and Thermal Properties of Sphalerite CuZn₂InS₄. *Dalt. Trans.* **2021**, *50* (47), 17611–17617.
- (63) Gunatilleke, W. D. C. B.; Juneja, R.; Ojo, O. P.; May, A. F.; Wang, H.; Lindsay, L.; Nolas, G. S. Intrinsic Anharmonicity and Thermal Properties of Ultralow Thermal Conductivity Ba₆Sn₆Se₁₃. *Phys. Rev. Mater.* **2021**, *5* (8), 085002.
- (64) Certain commercial equipment, instrumentation, or materials are identified in this document to adequately specify the experimental procedures. Such identification does not imply recommendation or endorsement by the National Institute of Standards and Technology, nor does it imply that the products identified are necessarily the best available for the purpose.
- (65) Toby, B. H.; Von Dreele, R. B. GSAS-II: The Genesis of a Modern Open-Source All Purpose Crystallography Software Package. *J. Appl. Crystallogr.* **2013**, *46* (2), 544–549.
- (66) Martin, J.; Erickson, S.; Nolas, G. S.; Alboni, P.; Tritt, T. M.; Yang, J. Structural and Transport Properties of Ba₈Ga₁₆Si_xGe_{30-x} Clathrates. *J. Appl. Phys.* **2006**, *99* (4), 044903.
- (67) Martin, J.; Nolas, G. S. Apparatus for the Measurement of Electrical Resistivity, Seebeck Coefficient, and Thermal Conductivity of Thermoelectric Materials between 300 and 12 K. *Rev. Sci. Instrum.* **2016**, *87* (1), 015105.
- (68) Giannozzi, P.; Baroni, S.; Bonini, N.; Calandra, M.; Car, R.; Cavazzoni, C.; Ceresoli, D.; Chiarotti, G. L.; Cococcioni, M.; Dabo, I.; Dal Corso, A.; De Gironcoli, S.; Fabris, S.; Fratesi, G.; Gebauer, R.; Gerstmann, U.; Gougaussis, C.; Kokalj, A.; Lazzeri, M.; Martin-Samos, L.; Marzari, N.; Mauri, F.; Mazzarello, R.; Paolini, S.; Pasquarello, A.; Paulatto, L.; Sbraccia, C.; Scandolo, S.; Sclauzero, G.; Seitsonen, A. P.; Smogunov, A.; Umari, P.; Wentzcovitch, R. M. QUANTUM ESPRESSO: A Modular and Open-Source Software Project for Quantum of Materials. *J. Phys.: Condens. Matter* **2009**, *21* (39), 395502.
- (69) Perdew, J. P.; Burke, K.; Ernzerhof, M. Generalized Gradient Approximation Made Simple. *Phys. Rev. Lett.* **1996**, *77* (18), 3865.
- (70) Perdew, J. P.; Ernzerhof, M.; Burke, K. Rationale for Mixing Exact Exchange with Density Functional Approximations. *J. Chem. Phys.* **1996**, *105* (22), 9982.
- (71) Cococcioni, M.; De Gironcoli, S. Linear Response Approach to the Calculation of the Effective Interaction Parameters in the LDA+U Method. *Phys. Rev. B* **2005**, *71* (3), 035105.
- (72) Blöchl, P. E. Projector Augmented-Wave Method. *Phys. Rev. B* **1994**, *50* (24), 17953–17979.
- (73) Agapito, L. A.; Curtarolo, S.; Buongiorno Nardelli, M. Reformulation of DFT + U as a Pseudohybrid Hubbard Density Functional for Accelerated Materials Discovery. *Phys. Rev. X* **2015**, *5* (1), 011006 and references therein.
- (74) Momma, K.; Izumi, F. VESTA: A Three-Dimensional Visualization System for Electronic and Structural Analysis. *J. Appl. Crystallogr.* **2008**, *41* (3), 653–658.
- (75) Matje, P.; Müller, W.; Schäfer, H. Zur Darstellung Und Kristallstruktur von Ba₂MnTe₃. *Z. Naturforsch. - Sect. B J. Chem. Sci.* **1977**, *32* (7), 835–836.
- (76) Brese, N. E.; O'Keeffe, M. Bond-Valence Parameters for Solids. *Acta Crystallogr.* **1991**, *B47* (2), 192–197.
- (77) Kittel, C. *Introduction to Solid State Physics*, 5th ed.; John Wiley & Sons, Inc., 1976.
- (78) Ghosh, T.; Dutta, M.; Sarkar, D.; Biswas, K. Insights into Low Thermal Conductivity in Inorganic Materials for Thermoelectrics. *J. Am. Chem. Soc.* **2022**, *144* (23), 10099–10118.
- (79) Koumpouras, K.; Larsson, J. A. Distinguishing between Chemical Bonding and Physical Binding Using Electron Localization Function (ELF). *J. Phys.: Condens. Matter* **2020**, *32* (31), 315502.
- (80) Pal, K.; He, J.; Wolverton, C. Bonding Hierarchy Gives Rise to High Thermoelectric Performance in Layered Zintl Compound BaAu₂P₄. *Chem. Mater.* **2018**, *30* (21), 7760–7768.
- (81) Zhang, J.; He, D.; Jiang, H.; Xia, X.; Gao, Y.; Huang, Z. Remarkable Thermoelectric Performance in K₂CdPb Crystals with 1D Building Blocks via Structure Particularity and Bond Heterogeneity. *ACS Appl. Energy Mater.* **2022**, *5* (4), 5146–5158.
- (82) Pal, K.; Xia, Y.; He, J.; Wolverton, C. High Thermoelectric Performance in BaAgYTe₃ via Low Lattice Thermal Conductivity Induced by Bonding Heterogeneity. *Phys. Rev. Mater.* **2019**, *3* (8), 085402.